ADVANCED MATERIALS INTERFACES
Open Access
www.advmatinterfaces.de

Resolving Diverse Oxygen Transport Pathways Across Sr-Doped Lanthanum Ferrite and Metal-Perovskite Heterostructures

Sandra D. Taylor, Kayla H. Yano,* Michel Sassi, Bethany E. Matthews, Elizabeth J. Kautz, Sten V. Lambeets, Sydney Neuman, Daniel K. Schreiber, Le Wang, Yingge Du, and Steven R. Spurgeon**

Perovskite structured transition metal oxides are important technological materials for catalysis and solid oxide fuel cell applications. Their functionality often depends on oxygen diffusivity and mobility through complex oxide heterostructures, which can be significantly impacted by structural and chemical modifications, such as doping. Further, when utilized within electrochemical cells, interfacial reactions with other components (e.g., Ni- and Cr-based alloy electrodes and interconnects) can influence the perovskite's reactivity and ion transport, leading to complex dependencies that are difficult to control in real-world environments. Here, this work uses isotopic tracers and atom probe tomography to directly visualize oxygen diffusion and transport pathways across perovskite and metal-perovskite heterostructures, that is, (Ni-Cr coated) Sr-doped lanthanum ferrite ($La_{0.5}Sr_{0.5}FeO_3$; LSFO). Annealing in $^{18}O_{2(g)}$ results in elemental and isotopic redistributions through oxygen exchange (OE) in the LSFO while Ni-Cr undergoes oxidation via multiple mechanisms and transport pathways. Complementary density functional theory calculations at experimental conditions provide rationale for OE reaction mechanisms and reveal a complex interplay of different thermodynamic and kinetic drivers. These results shed light on the fundamental coupling of defects and oxygen transport in an important class of catalytic materials.

1. Introduction

Perovskite structured transition metal oxides (general chemical formula of ABO_3) are widely studied in chemistry and condensed matter physics, owing to their strong coupling among lattice, spin, and orbital degrees of freedom.[1] These crystals can accommodate a variety of property-defining cation species, giving rise to diverse electronic, magnetic, and optical behavior.[2] For instance, their catalytic activity and properties can be significantly influenced by substitution or partial substitution of the A- and/or B-site cations.[3–6] Among the many perovskites being pursued for catalytic applications, Sr-doped lanthanum ferrites ($La_{1-x}Sr_xFeO_3$; LSFO) have attracted particular attention for photocatalytic water splitting,[7–10] with Fe as the B-site transition metal cation driving selective oxidation. The La^{3+} cations are substituted by cations in a lower oxidation state (i.e., Sr^{2+}), leading to the partial oxidation of the B cations to a higher oxidation state and/or to the formation of oxygen vacancies, which results in better catalytic activity.[10] The perovskite's ability to accommodate a range of substituents and dopants provides significant flexibility in its composition and associated oxidation state. This tunability in turn enables tailoring of the perovskite's physicochemical properties for various applications such as cathode materials in solid oxide fuel cells (SOFCs), catalysts and oxygen carriers in heterogeneous catalysis, oxygen separation membranes, and solid-state gas sensors.[11]

S. D. Taylor, M. Sassi, S. V. Lambeets, L. Wang, Y. Du
Physical and Computational Sciences Directorate
Pacific Northwest National Laboratory
Richland, WA 99352, USA
E-mail: sandra.taylor@pnnl.gov

The ORCID identification number(s) for the author(s) of this article can be found under https://doi.org/10.1002/admi.202202276.

DOI: 10.1002/admi.202202276

K. H. Yano, B. E. Matthews, E. J. Kautz, S. Neuman, D. K. Schreiber, S. R. Spurgeon
Energy and Environment Directorate
Pacific Northwest National Laboratory
Richland, WA 99352, USA
E-mail: steven.spurgeon@pnnl.gov

S. R. Spurgeon
Department of Physics
University of Washington
Seattle, WA 98195, USA

The mobility of oxygen ions is a key parameter affecting a perovskite's reactivity and functionality across these applications.[12] Diffusion through the oxide bulk follows a vacancy-mediated mechanism, where transport occurs by discrete hops of oxygen anions to neighboring vacancies.[10] Diffusion rates can be further manipulated by modifying vacancy or other defect populations via cation doping.[13–15] Further, as mixed ionic-electronic conductors, oxygen from the environment can reversibly adsorb/desorb into the lattice and exchange by continuous changes in oxidation state, without changes to the bulk crystal structure.[10,16,17] However, the oxygen exchange (OE) reaction itself consists of numerous elementary steps and reaction sequences, such as oxygen adsorption, reduction and dissociation, diffusion of the disassociated species, and subsequent incorporation into the host (cathode/electrolyte) lattice,[18] which have yet to be fully understood.

Within designed electrochemical cells, ion transport is also influenced by synergistic reactions with the various components of the electrode and interconnects. For instance, in the design of intermediate temperature (600–800 °C) SOFCs, chromia-forming stainless steel interconnects are desirable due to the higher electronic and thermal conductivity, lower cost, and easier fabrication than traditional ceramic parts.[19–21] However, a significant challenge in their application is the severe degradation of the cathode performance resulting from poisoning via Cr-species evaporated from the interconnect alloy oxide scale. Deposition of Cr-species blocks active sites on the electrode surface, negatively affecting charge transfer and oxygen diffusion,[19] although the specific controlling mechanisms are convoluted and poorly understood.[22] Knowledge of oxygen reactivity and transport pathways in the oxide catalyst and relative to components of the electrochemical cell can provide fundamental insight into degradation mechanisms, guiding cell design to optimize performance.

In this study, we directly resolve oxygen transport pathways across (metal-)perovskite heterostructures at the nanoscale to gain insight into diffusivity and surface exchange reactions. To do so, oxygen diffusion was studied within LSFO (i.e., $La_{0.5}Sr_{0.5}FeO_3$ grown on (001) $[LaAlO_3]_{0.3}[Sr_2AlTaO_6]_{0.7}$, [LSAT]) and across a heterogeneous metal-LSFO system (Ni- and Cr-metal). LSFO serves as a model system to study vacancy-mediated oxygen transport in the bulk, as rapid diffusion was previously measured although this has not been directly resolved at the nanoscale.[13,23] Thin films of Ni and Cr deposited on top of the LSFO serve as surrogate interfaces for metallic anodes and interconnects in electrochemical cells.[24] Recently developed isotopic tracer techniques with atom probe tomography (APT) were employed to resolve elemental and isotopic distributions in 3D with sub-nanometer resolution.[25–28] That is, APT specimens were prepared and annealed in gaseous ^{18}O-enriched oxygen gas using the in situ atom probe (ISAP) method.[29] In turn, APT analysis highlights oxygen mobility through the perovskite phase, and complementary ab initio simulations provide further insight into the inherent properties and thermodynamic driving forces for ion transport. Further, local changes in the elemental and isotopic distributions across the metal and perovskite phases after annealing reveal unique oxygen transport pathways and mechanisms across the heterostructure. These observations are key to understanding mass transport phenomena controlling the degradation, rejuvenation, and stability of complex perovskite catalysts and oxide heterostructures.

2. Results and Discussion

2.1. Baseline Characterization of As-Grown Sample

$La_{0.5}Sr_{0.5}FeO_3$ films nominally ≈9 nm thick (≈22-unit cells) were epitaxially grown on (001)-oriented LSAT substrates using pulsed laser deposition. Cr- and Ni-layers (≈15 and ≈30 nm, respectively) were then deposited on the LSFO surface via ion beam sputtering deposition (IBSD) at room temperature. The baseline microstructure of the metal-perovskite heterostructure was established by high-resolution scanning transmission electron microscopy (STEM) high-angle annular dark field (HAADF) imaging, as shown in **Figure 1**. Atomic resolution imaging confirms the epitaxial and single crystal nature of the LSFO thin films on the highly crystalline-LSAT substrate. The sputtered Ni and Cr metal layers are nanocrystalline, as

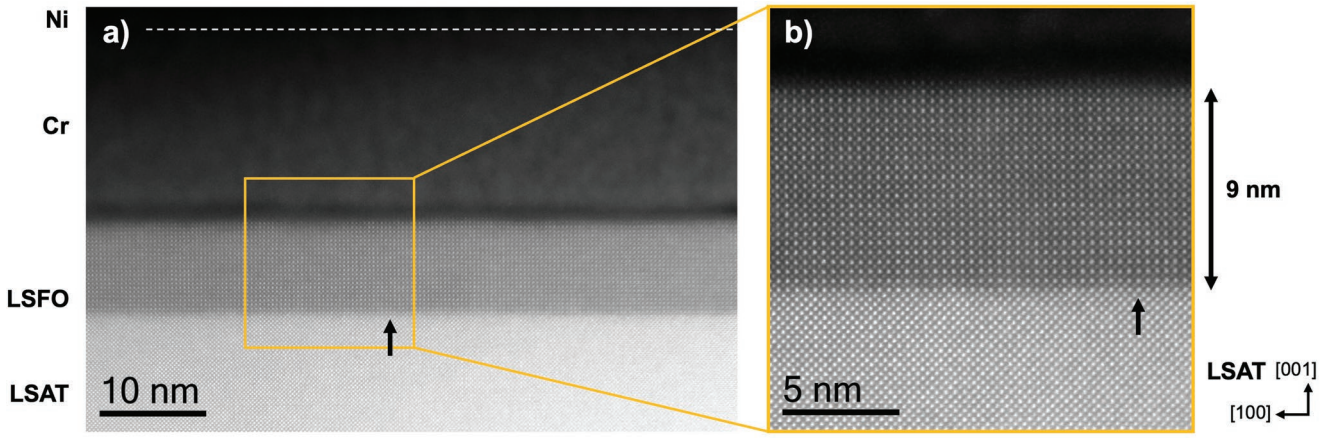

Figure 1. Cross-sectional STEM-HAADF imaging of a) the Ni-Cr-LSFO-LSAT heterostructure taken along the LSAT [010] zone, and b) the LSFO and LSAT structure with black arrows indicating steps in the substrate.

expected. The LSFO film structure is largely uniform with few to no microscopic defects (with the exception of some steps near the LSFO-LSAT interface) (Figure 1b), though oxygen vacancy concentrations are expected to be significant at this level of Sr-doping.[14]

The elemental and isotopic composition of the as-grown metal-perovskite stack was characterized by APT (see Experimental Section and Supporting Information for details on APT sample preparation as well elemental and isotopic analyses; Figures S1–S3, Table S1, Supporting Information). We note that two APT specimens were analyzed for each experiment, where one specimen from each experiment is shown in the main text as a representative sample (elemental and isotopic analyses of the remaining specimens are provided in Figure S4, Supporting Information). 3D chemical reconstructions of the as-grown specimen clearly show the unique stack geometry and chemistry of the metal-perovskite system (**Figure 2**a). The baseline compositions of the phases are in reasonable agreement with that expected (Figure 2b, Table S1, Supporting Information). That is, the Ni and Cr coatings are largely metallic (77.7 ± 2.5 atomic % (at%) Ni and 70.6 ± 1.5 at% Cr, respectively, based on the average composition and standard deviation across the two APT tips measured). Oxygen is present in both layers (13.3 ± 1.5 at% and 21.6 ± 1.2 at% in both Ni and Cr layers, respectively), which is present in the IBSD chamber during deposition.[25] Aluminum, an impurity introduced by Al components in the sputter system, is also present at low concentrations (6.8 ± 1.5 at% and 6.6 ± 0.3 at% in Ni and Cr layers, respectively).

Quantification of the as-grown LSFO composition shows that Fe is the primary cation (27.2 ± 0.1 at% Fe) followed by Sr and then La (18.5 ± 0.4 at% and 10.7 ± 0.5 at%, respectively). The measured O concentration is only 43.3 ± 0.9 at% versus the expected concentration of 60 at% O of the ABO_3 stoichiometry. While some of this O deficiency could reflect oxygen vacancies due to the Sr-doping, it is important to note that oxygen quantification is inherently challenging in APT,[30,31] especially in Fe-base oxides.[25,30,32–34] We can nonetheless follow changes in concentrations before and after annealing to determine relative composition changes. The APT-measured as-grown LSAT composition (7.6 at% La, 14.1 at% Sr, 10.0 at% Al, 8.5 at% Ta, and 58.7 at% O, based on the composition from one APT specimen) is in reasonable agreement with expectations (3.6 at% La, 16.4 at% Sr, 11.8 at% Al, 8.2 at% Ta, and 60 at% O). APT analyses along the defined [001] direction of the LSFO film show a homogeneous composition along the depth of each phase, with little to no elemental intermixing as demarcated by the sharp interfaces between phases (Figure 2a-b).

The oxygen isotopic composition of each phase and across the heterostructure was determined using a single, consistent

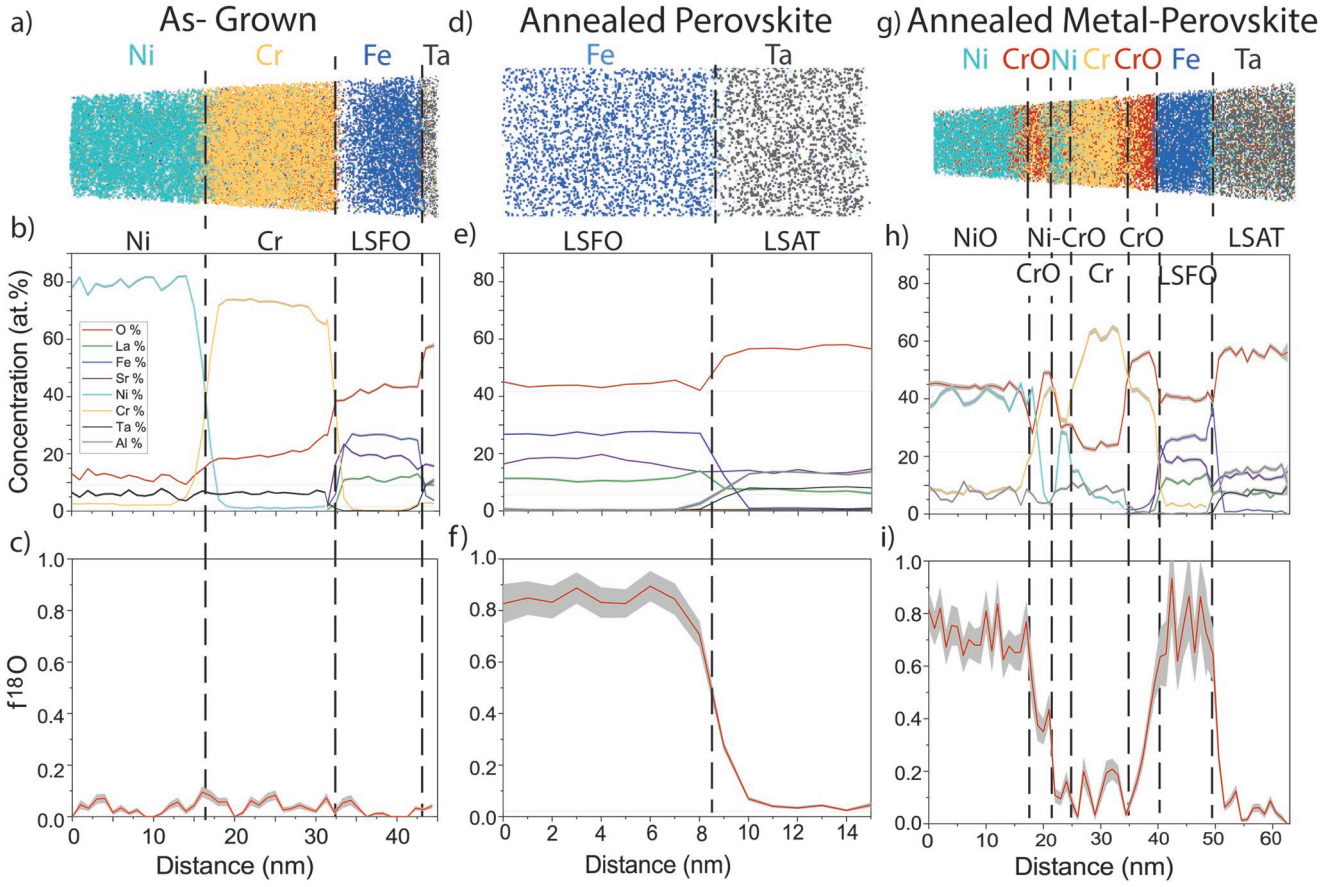

Figure 2. APT reconstructions, elemental profiles, and $f^{18}O$ for the a–c) as-grown versus d–f) annealed perovskite versus g–i) annealed metal-perovskite specimens. Shading is used to highlight the uncertainty associated with the counting statistics (1σ, see Experimental Section).

species, that is, O^{1+} species (16–18 Da). This avoided potential interferences given the multi-isotopic and elemental nature of this system (see Experimental Section and Supporting Information for details on ^{18}O analytical protocols, Figure S3, Supporting Information), The oxygen composition is expressed as the fraction of ^{18}O relative to ^{16}O and ^{18}O ($f^{18}O$).[25] The average $f^{18}O$ measurements for the bulk Ni, Cr, LSFO, and LSAT were 0.05 ± 0.02, 0.04 ± 0.00(1), 0.01 ± 0.00(4), and 0.01 respectively (Figure 2c, Table S1, Supporting Information). These $f^{18}O$ measurements within each phase of the as-grown specimen are within reason of that expected for natural abundance (NA) (0.002); the presence of hydrogen in the APT analysis chamber leads to the slight deviations.[35] Nonetheless, these measurements show the oxygen isotopic composition within the as-grown specimen is effectively at NA. As shown shortly, following annealing, changes in $f^{18}O$ are significant and thereby can be used to reliably infer oxygen diffusivity and reactions across the stack.

2.2. Oxygen Mobility in the Annealed-Perovskite System

To isolate and deduce oxygen mobility in perovskite based on its inherent properties, APT specimens of the as-grown sample were prepared such that the Ni-Cr overlayer was evaporated (by APT)—leaving only the LSFO-LSAT phases. The specimens were annealed in $^{18}O_{2(g)}$ (400 °C, 4 h, 3 mbar, 99 at% purity, Sigma Aldrich) using the ISAP method, described in detail elsewhere,[29] and were then transferred under vacuum for APT analysis (hereafter referred to as the annealed perovskite specimens). The elemental and isotopic compositions were then assessed to determine whether phase alteration occurred. The elemental compositions of the annealed LSFO and LSAT layers are consistent with their as-grown counterparts (Figure 2d–f, Table S1, Supporting Information). Notably, the O concentration in the annealed LSFO is within variability of the as-grown measurements (43.8 ± 0.3 at% vs 43.3 ± 0.9 at%, respectively), indicating there is no net addition or removal of oxygen during reaction.

Though elemental analyses indicate phase alteration does not occur, the oxygen isotopic composition demonstrates that lattice oxygen in the LSFO nearly completely exchanges with the ^{18}O-enriched environmental O_2 (Figure 2f, Table S1, Supporting Information). Quantitatively, the LSFO $f^{18}O$ increases from 0.01 ± 0.0(04) in the as-grown specimen to 0.84 ± 0.01 after annealing. In comparison LSAT does not experience OE, remaining near NA ($f^{18}O$ = 0.04). Additionally, isotopic measurements along [001] indicate OE is homogeneous along the depth of the LSFO film. Elemental composition analyses also show that the LSFO and LSAT exhibit no evidence of phase transformations.

While OE in perovskites has not been measured previously at these modest temperatures, the extent of exchange seems reasonable based on rough predictions for oxygen diffusivity in LSFO and surface exchange to occur. Arrhenius extrapolations of $La_{0.6}Sr_{0.4}FeO_3$ estimate oxygen diffusivity at 400 °C to be ≈10^{-18} m^2 s^{-1} or 1 nm^2 s^{-1},[13] and would yield a characteristic diffusion distance of ≈240 nm over the 4 h anneal. These film dimensions are significantly smaller than this distance (i.e., ≈9 nm thick and <100 nm in diameter; Figure S1, Supporting Information) and thus suggest oxygen diffusion could occur through the entirety of the film, consistent with the extensive OE we observe. Additionally, the needle-shaped APT specimen geometry and large surface area exposed (estimated to be on the order of 10^3–10^4 nm^2) could facilitate OE via surface exchange (see Supporting Information for more information on the physical measurements, Figure S1, Supporting Information). For example, $LaFeO_3$ (LFO) annealed in $^{18}O_{2\,(g)}$ at >900 °C showed the most OE occurs near the surface and decreases into the bulk, based on limited observations from lower-resolution isotopic exchange depth profile measurements with secondary ion mass spectrometry (i.e., >100 nm).[23]

2.3. Oxygen Exchange Mechanisms

Oxygen transport and exchange in LSFO is ultimately controlled by the behavior and concentration of oxygen vacancies.[18] Our experimental observations are consistent with this (e.g., the highly-crystalline LSAT is unreactive while extensive oxygen diffusion and exchange in LSFO reflects inherently high defect concentrations). To support the experimental observations, atomistic modeling was used to further probe the vacancy-mediated transport mechanisms and driving forces at play. Specifically, the thermodynamic stability and migration energy barriers of oxygen vacancies in LSFO were simulated and quantified using density functional theory (DFT). The thermodynamic stability was first probed using ab initio thermodynamics calculations that can incorporate the effects of various experimental conditions (e.g., oxygen partial pressure, temperature, chemical potential differences between oxygen isotopes, and Sr concentrations). Subsequently the energetic drivers and migration barriers for vacancy-mediated transport, thought to influence the incorporation/removal of lattice oxygen and diffusion, were further evaluated.

The calculation of the Gibbs free energy of formation of an oxygen vacancy in LSFO indicates that heating increases the instability of vacancies. As shown in **Figure 3**a, the Gibbs free energy of oxygen vacancy formation is less favorable at high temperature than at room temperature for a O_2-partial pressure of 3 mbar. Since creating an oxygen vacancy is less energetically favorable (or more costly) at high temperature, the thermodynamic driving force for filling a vacancy is more important than at room temperature. This may be a potential driver for oxygen incorporation into the lattice. The degree of instability introduced by heating is also affected by the oxygen partial pressure, such that an increase in pO_2 further increases the instability of oxygen vacancies. At the oxygen partial pressure used in this study (pO_2 = 3 mbar), oxygen vacancies are found to be 1.31 eV less stable at 400 °C (673 K) than at ambient temperature. This thermodynamically favors oxygen ingress from the environment to occupy oxygen vacancies. Countering this tendency, the vacancy concentration in the material is also restrained and maintained by the perovskite composition (i.e., Sr doping); our experimental observations are nominally consistent with this notion, as the oxygen concentration (an indirect indication of vacancy content) does not change during reaction. Thus, while annealing makes oxygen vacancies less energetically favorable thermodynamically, a steady-state vacancy concentration is maintained throughout the reaction.

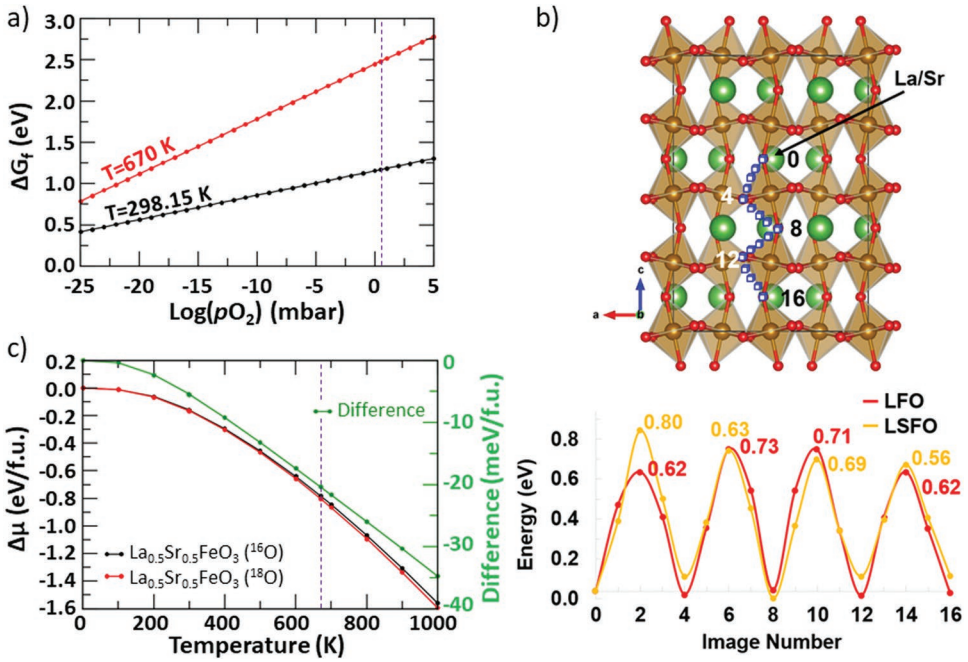

Figure 3. a) Gibbs free energy of oxygen vacancy formation in LSFO ($x = 0.5$) as function of pO_2 for temperatures of 25 (298 K) and 400 °C (673 K). The vertical dashed line indicates the experimental pO_2 (3 mbar). b) Impact of a single Sr substitution on the migration energy barrier of an oxygen vacancy. The pathway investigated is indicated by blue squares. When Sr is introduced, the initial image configuration (position 0) corresponds to an oxygen vacancy being first neighbor with the Sr species. The energy barriers have been calculated relative to the local minima just prior to the transition state. c) Comparison of the chemical potential (per formula unit) of LSFO for a compound made of two different O isotopes, either ^{16}O or ^{18}O. The chemical potential difference is shown by the green curve and right *y*-axis in meV/f.u. The vertical dashed line indicates the temperature at which experiments have been performed.

To understand oxygen diffusion via vacancy-hopping mechanisms, the energetics for oxygen vacancy migration in the perovskite lattice were calculated using the climbing image nudged elastic band (CINEB) method. To quantify the impact of Sr doping on the oxygen vacancy migration energy barrier as a function of the Sr/O-vacancy separation distance (Figure 3b), we used a supercell where one La atom was substituted by a Sr atom and compared it to oxygen vacancy migration in LFO. In the case of pure LFO, the highest calculated energy barrier is 0.73 eV, in good agreement with previously reported experimental and theoretical values of ≈0.70–0.80 eV.[12,13,36] However, when Sr is present in the lattice, the migration of a first neighbor oxygen vacancy away from Sr must overcome a first energy barrier of 0.80 eV, compared to 0.62 eV for pure LFO. While subsequent energy barriers along the pathway are smaller, ranging from 0.56 to 0.69 eV, this indicates that oxygen vacancies are more strongly associated with Sr. The trend obtained is in good agreement with the literature, suggesting that the energy barrier for the migration of the oxygen vacancy increases with the Sr fraction.[36–38] However, these high energetic barriers seemingly contradict observations from diffusion studies, as oxygen diffusion increases with Sr doping (e.g., bulk diffusion in $La_{1-x}Sr_xFeO_3$ [$x = 0.4$, 1000 °C] was measured to be 4–5 orders of magnitude faster than that in pure LFO).[13,36–38] This suggests that the impact of Sr doping on the concentration of oxygen vacancies is a more important factor driving oxygen migration than its associated cost to the energy barrier. Therefore, high vacancy concentrations predominantly control oxygen diffusivity in LSFO, irrespective of the energetic barriers for vacancy migration, and enable long-range oxygen diffusion and migration.

To provide a rationale for the significant OE observed, bulk thermodynamic calculations for LSFO composed of either ^{16}O or ^{18}O were performed as function of temperature to evaluate the impact of isotope substitution on the chemical potential of LSFO. At 400 °C, a difference of 20 meV/formula unit (1 formula unit = $La_{0.5}Sr_{0.5}FeO_3$ or 6.67 meV/O atom) in favor of the ^{18}O-LSFO compound is obtained (Figure 3c). The thermodynamic preference for ^{18}O is not due to a change in enthalpy, as ^{16}O and ^{18}O are the same chemical species with the same number of valance electrons, but to a difference in their mass which impacts their respective contribution to vibrational entropy. Based on this difference, the calculation of the Boltzmann factor to approximate the fraction of ^{18}O yields to 70% if we consider the energy gain per formula unit or 89% if we use the energy gain per O atom. On average, this approximation suggests that LSFO would favor the near complete replacement (≈80%) of lattice ^{16}O by ^{18}O, which is consistent with our experimental observations. The influence of isotopic mass in combination with the thermodynamic instability of vacancies at 400 °C and $pO_2 = 3$ mbar highlights some of the potential driving forces for OE.

2.4. Oxygen Mobility in Annealed Metal-Perovskite

Knowing the mobility and reactivity of oxygen in the perovskite system, APT specimens of the as-grown sample—with the Ni and Cr-metal intact with LSFO—were annealed at the same conditions (hereafter referred to as annealed metal-perovskite

specimens) and analyzed to determine how the metallic overlayers influence ion transport. Elemental analyses of the annealed metal-perovskite specimens indicates that the LSFO and LSAT phases effectively remain the same (Figure 2g,h; Table S1, Supporting Information), as observed in the annealed perovskite case (Figure 2d,e; Table S1, Supporting Information). That is, LSAT has not undergone any chemical change or isotopic exchange, again demonstrating it is effectively inert. The bulk LSFO elemental composition is similar to the annealed-perovskite (and as-grown) specimen, and there is no net oxygen concentration change during reaction (42.3 ± 0.0(3) at% O). Oxygen isotopic analysis also shows near complete OE in LSFO, like that in the perovskite-annealed specimens (f^{18}O 0.82 ± 0.07 vs 0.84 ± 0.01, respectively).

The elemental and oxygen isotopic composition of the Ni and Cr layers overlying LSFO have changed significantly following annealing, indicative of metal oxidation and phase transformation (Figure 2g,h; Table S1, Supporting Information). That is, Ni has clearly oxidized, as the oxygen concentration in the Ni layer has increased from 13.3 ± 1.5 at% in the as-grown to 44.0 ± 0.4 at% after annealing, suggestive of a NiO-like phase. The Cr-layer has also partially oxidized following annealing, primarily at its interfaces with other layers; i.e., Cr-rich oxides, similar to Cr_2O_3,[39] formed near the Ni (≈45 at% Cr, 50 at% O) and LSFO phases (≈40 at% Cr, ≈60 at% O) (Figure 2). The Cr bulk experiences less oxidation relative to the interfaces and is largely metallic (e.g., only ≈25 at% O), like the as-grown material. It is important to note that the specimen outer surface is not included in the APT reconstruction as this was outside the field of view; i.e., the field of view captures the central volume of the specimen, and is estimated to capture ≈55% of the specimen (see Supporting Information for details, Figure S1, Supporting Information).[40] However, we expect the exposed Cr surfaces to have also oxidized given its direct exposure to oxygen gas at elevated temperatures. Oxidation of both Ni and Cr is rational as it is thermodynamically favorable at these conditions.[41] Interestingly, the formation of Cr oxide particularly, within the field of view, seems to allude to unique reaction pathways at the interfaces, as explored shortly by oxygen isotopic analyses.

Some elemental mixing between the Ni and Cr regions has also occurred, as a thin mixed Ni-Cr oxide layer is now present between the Cr-rich oxide (near the Ni-Cr interface) and the Cr-bulk. In comparison, cation intermixing (i.e., mixed oxides) is not found at the Cr-LSFO interface. Prior work on the oxidation behavior of a Ni-Cr alloys indicated the initial stage of oxidation involved the formation of an outward growing mixed Ni-Cr oxide due to the rapid movement of cations, like Ni.[42–44] Later stages indicate a Cr-rich inward growing oxide layer formed via migration of O from the environment moving toward the metal interfaces and along grain boundaries. Due to this partitioning of the oxide observed in prior studies, we speculate the formation of the embedded Ni-Cr oxide is due to interdiffusion of the cation species during annealing and oxidation.

Oxygen isotopic analyses of the different Ni and Cr oxide phases within the central volume of the APT specimen (i.e., within our field of view) suggest oxidation occurs via different pathways. That is, f^{18}O in the Ni layer has increased from 0.05 ± 0.02 in the as-grown specimen to 0.78 ± 0.07 after annealing (Figure 2c,i), indicating that oxidation occurs from

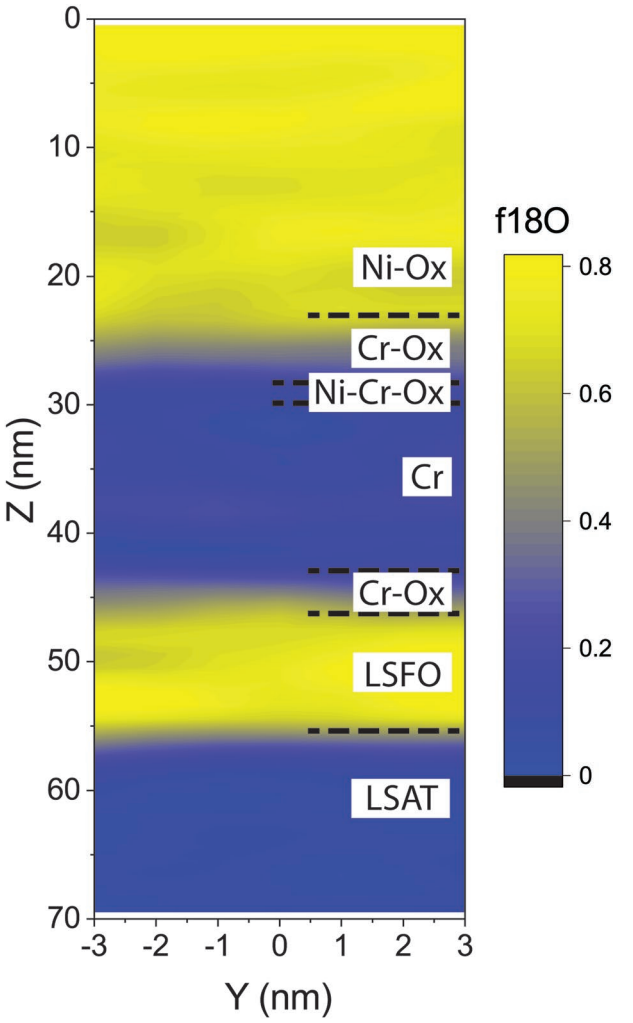

Figure 4. 2D heat map showing the oxygen isotopic composition across the annealed metal-perovskite specimen.

gaseous ^{18}O from the environment. Measurements and visualization of the oxygen isotopic distribution also show ^{18}O homogeneously distributed over the Ni phase (Figure 2i, **Figure 4**). In comparison, the oxygen isotopic composition throughout the mixed Ni-Cr oxide is effectively the same as that in the as-grown specimens (0.11 ± 0.02) (Figure 2i, Figure S4i, Supporting Information). This seemingly suggests the oxide forms from oxygen originally present in the metal layer, not gaseous ^{18}O from the environment.

Isotopic analyses of the Cr-oxides formed at the interfaces reveal a gradient in ^{18}O and allude to yet another transport pathway. That is, for the Cr oxide near LSFO, f^{18}O is highest near the LSFO interface and decreases approaching the Cr bulk (from 0.70 ± 0.05 to 0.10 ± 0.10) (Figure 2i, Figure 4). Similar observations are made for the Cr-oxide near the Ni oxide phase (f^{18}O decreases from 0.38 ± 0.08 at the interface to 0.08 ± 0.04 toward the Cr-bulk). The ^{18}O distribution across the interfaces are also noticeably diffuse (Figure 4). The oxygen isotopic content in the bulk Cr phase is largely ^{16}O (f^{18}O = 0.15 ± 0.10) and homogeneous. These observations suggest that Cr within the central volume of the APT specimen,

within our field of view, is neither simply oxidized by gaseous oxygen from the environment or by oxygen originally present in the metal layers. Based on the $f^{18}O$ gradients, we hypothesize that Cr oxide is formed from the reaction of Cr with oxygen anions at these interfaces with LSFO and the Ni.

Interpretation of the mass transport phenomena across these interfaces is complicated, having to consider thermodynamics, kinetics (i.e., ion mobilities), and transport mechanisms in each phase and in relation to one another. It is important to first limit our discussion to that observed within our field of view, the center of the APT specimen. Likely, Cr oxide forms at the Ni oxide and LSFO interfaces by ion diffusion. As shown in both the annealed perovskite and metal-perovskite specimens, oxygen diffusion is a dominant process in LSFO. However, interpretation of the oxygen behavior and mobility within the Ni and Cr (oxides) is complicated by the metal oxidation reaction. That is, during oxidation of the Ni and Cr metallic phases, oxygen will react to form NiO and Cr_2O_3, respectively, as it is thermodynamically favorable.[41] Oxygen will not freely diffuse in the metal.

Following formation of the Ni and Cr oxides, oxygen diffusion can be considered. Extrapolating the Arrhenius expressions from previous high temperature studies to 400 °C,[45,46] the oxygen diffusivity in NiO and Cr_2O_3 would be predicted to be $\approx 10^{-19}$ and 10^{-36} m^2 s^{-1}, respectively. For this study, this would yield characteristic diffusion distances on the order of ≈10 versus 10^{-7} nm in NiO and Cr_2O_3, respectively, after 4 h. This suggests oxygen would be immobile in bulk Cr oxide while it readily diffuses in LSFO and may diffuse at the nanometer-scale in Ni oxide. Rather, based on previous studies attributing metal oxidation to cationic diffusion, Cr oxide may instead form by Cr diffusing to and consuming oxygen at the oxide interfaces.[47] Our observations of Cr oxide forming between the Ni and Ni-Cr oxides suggest cation diffusion occurs. Further, if we expand our hypothesis to what is occurring outside the field of view, we expect Cr along the surface of the APT specimen is oxidized by the gaseous environment. The passivating Cr-oxide film could prevent ^{18}O ingress from the sides of the APT specimen, whereas the Ni (NiO) and LSFO are relatively O permeable. This would make the NiO and LSFO the predominant O sources for Cr oxidation within our field of view.

3. Conclusions

Our combined elemental and isotopic observations across the as-grown, annealed perovskite, and annealed metal-perovskite specimens reveal diverse oxygen transport pathways across the system, controlled by the unique reactivity and relationships between phases. This includes 1) exchange between oxygen in LSFO lattice and the gaseous environment, 2) Ni oxidation by gaseous $^{18}O_2$ from the environment, and 3) Cr oxidation via oxygen from the neighboring NiO and LSFO phases (**Figure 5**).

Extensive OE in LSFO is consistent with vacancy-mediated mechanisms, where transport and exchange occurs by discrete hops of oxygen ions to neighboring vacant sites and, in this case, leads to the near complete replacement of lattice ^{16}O with ^{18}O from the environment. The consistent oxygen concentrations

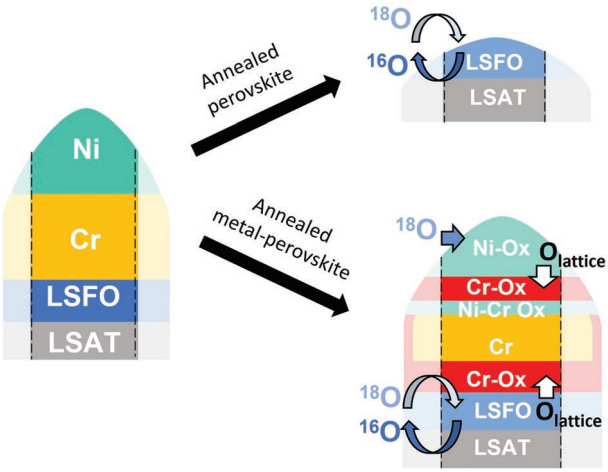

Figure 5. Conceptual schematic of the diverse oxygen transport pathways and reactions, highlighting OE between lattice oxygen in LSFO and $^{18}O_{2(g)}$ coupled with oxidation of the metallic layers. Vertical dashed lines denote the conceptual field of view captured by APT; we hypothesize that the oxidation and passivation of the Cr also occurred over the exposed tip surfaces outside the field of view (denoted by the translucent regions at the shanks).

in the LSFO for the perovskite-annealed and metal-perovskite annealed specimens relative to the as-grown specimen suggest that steady-state composition is reached, as there is no net addition or removal of oxygen in the LSFO layer (Figure 2). The theoretical simulations performed provide a rationale for OE reaction mechanisms and highlight a complex interplay of different factors. The thermal instability of vacancies, further enhanced by high O_2 partial pressure, provides a thermodynamic driver for oxygen atoms from the environment to occupy them. However, the composition (i.e., Sr doping) of the material forces the system to maintain a steady-state vacancy concentration throughout the reaction. While the concentration of oxygen vacancies is dictated by the degree of Sr doping, we propose that defect concentration is the main driver for lattice diffusion and that the increase of the migration energy barrier with Sr doping has a small impact on diffusion and exchange. In addition to the thermodynamics of defects and diffusion mechanisms, simulations showed that the isotopic substitution of ^{16}O in the LSFO lattice by ^{18}O lowers the chemical potential of the material, thereby favoring replacement.

Several parameters can contribute to the formation of the metal oxide films including thermodynamics of oxide formation, kinetics (i.e., ion mobility), and environmental parameters (oxygen partial pressure, presence of water vapor, temperature, etc.). Here, NiO is formed due to exposure to $^{18}O_2$ gas at elevated temperature, where oxygen partial pressure is higher and there is sufficient driving force for Ni oxidation.[48,49] Cr oxidation is also thermodynamically favorable (more so than other metal oxides including NiO).[41] However, the Cr oxide formed within the field of view, through the center of the APT specimen, is not simply due exposure to gaseous oxygen within the in situ reactor environment. Rather, we hypothesize oxygen from NiO and LSFO layers is consumed in the formation of a Cr oxide at the Ni(O)/Cr and Cr/LSFO interfaces. This is consistent based on the experimental measurements for the $f^{18}O$ gradient at the Ni oxide-Cr oxide and Cr oxide-LSFO interfaces.

Measurements and visualization of the oxygen isotope distribution at high-spatial and chemical resolution reveal different oxidation mechanisms and pathways for Ni versus Cr. While Cr-species will affect electrode performance by blocking active sites on the surface,[19] we show here that Cr can also potentially scavenge O from neighboring oxides. It also appears the oxide at least partially passivates, as the Cr metal layer did not fully oxidize, although this will depend on the cell's environmental conditions (e.g., temperature, oxygen pressure, etc.).

More broadly, this study demonstrates how the unique coupling of isotopic tracers with APT can provide insight into local, nanoscale reactions as well as potential reaction sequences. While this study was designed to investigate model heterostructures, this approach could be adapted to investigate engineering conditions and materials of interests to SOFCs and beyond at a variety of reaction conditions (e.g., temperature, time, oxygen pressure, etc.,). For instance, this approach can be applied to probe oxygen diffusion and exchange systematically, such as across LSFO heterostructures with varying dopants and doping concentrations. Further, the surface exchange and diffusion coefficients could be quantified at various temperatures by shortening the anneal time.[27] This can provide much-needed mechanistic insight into oxygen reactions with perovskites, which are of great significance as electrocatalysts with applications to oxygen reduction reactions. Our approach presents new opportunities to resolve oxygen reaction pathways across complex oxide heterostructures, which can inform fields from catalysis to corrosion science.

4. Experimental Section

Materials Synthesis: A detailed description of the LSFO growth procedure using pulsed laser deposition is provided in Stoerzinger et al., 2018.[9] In brief, the laser pulse (248 nm) energy density was ≈2 J cm^{-2} with a repetition rate of 1 Hz. During the deposition, the substrate was kept at 700 °C under an oxygen partial pressure of 10^{-2} mbar. After deposition, the samples were cooled to room temperature in 10^{-2} mbar oxygen. Ni and Cr films were sputter deposited onto LSFO using an IBSD system (IBS/e model, South Bay Technology Inc., San Clemente CA) at room temperature, using an Ar^+ ion beam source operating at 8 kV and 6 mA while maintaining a chamber pressure of 10^{-5} mbar during deposition.

Annealing Experiments: To probe oxygen transport across this system, an isotopic tracer was used during material processing to couple with APT analysis. APT specimens were annealed in ^{18}O-enriched oxygen gas (400 °C, 4 h, 3 mbar $^{18}O_2$; 99 at% purity, Sigma Aldrich) using the in ISAP method, detailed elsewhere.[29] This method allowed for the direct observation of sub-nanometer scale element redistributions at the specimen surface.[50–52] Briefly, this approach involved the direct exposure of APT specimens to a controlled gaseous environment at select pressures, temperatures, and times in a chemical reactor chamber attached directly to a commercial local electrode atom probe (LEAP) system.[29] The conditions were chosen such that oxygen transport across the thin film (≈10 nm) could be resolved by APT, based on extrapolations from previous studies; that is, oxygen diffusion at 400 °C was estimated to be ≈10^{-18} m^2 s^{-1} or 1 nm^2 s^{-1} when extrapolating diffusion measurements in $La_{0.6}Sr_{0.4}FeO_3$ from 900–1100 °C.[13] Following annealing, the specimens were transferred directly into the APT analysis chamber (within ≈2 min after ending the reaction) and were effectively quenched to ≈40–45 K within ≈30 min. This was all done under vacuum; i.e., the sample was transferred from the reactor to the analysis chamber at 10^{-7} mbar and cooled under ultra-high vacuum (10^{-11} mbar). Following cooling the specimens were analyzed.

APT Analyses: Samples were prepared for STEM and APT using conventional focused-ion beam scanning electron microscopy techniques (FIB-SEM; FEI Quanta 3D-FEG or Helios NanoLab dual-beam microscopes).[53,54] In particular, the APT specimens were prepared such that the final tip geometry consisted of Ni at the tip apex, underlain by Cr, LSFO, and LSAT, in sequence (see APT specimen preparation protocol in- Figure S1, Supporting Information). Microstructural and compositional characterizations of the thin film by both STEM and APT were done to get baseline measurements of the as-grown specimens.

APT samples were analyzed in a CAMECA LEAP 4000XHR at a base temperature of 40 K in laser-assisted field evaporation (λ = 355 nm) at pulse rates of 125 and 200 kHz. The laser pulse energy was set between 80 and 150 pJ and the detection rate was maintained at 0.002 detected ions per pulse by varying the applied voltage. The 3D APT reconstructions were done using the Integrated Visualization and Analysis Software (IVAS 3.8.5a45) with the shank angle approximation. APT reconstructions were scaled using STEM measurements of the film thicknesses and the interplanar spacing of the LSFO atomic bilayers that were also resolvable using spatial distribution maps. The oxygen bilayer spacing of LSFO as calculated by DFT is, on average, 1.95 Å in the [001] direction, and APT field evaporation and thus reconstruction captures every other of these bilayers (3.89Å). Using this scaling the films' thicknesses were consistent with that measured by STEM. Elemental and isotopic analyses were achieved through the careful assignment of ionic species best representative of the different phases (see Supporting Information for details on elemental and isotopic analyses, Figures S2 and S3; Table S1, Supporting Information).

Two APT specimens were analyzed for each condition (i.e., as-grown, annealed perovskite, and annealed metal-perovskite). Elemental concentrations were used to monitor potential phase transformations in the specimens after annealing in O_2. Isotopically resolved measurements were used to follow the provenance of oxygen from the reactor chamber (^{18}O) across the specimen as the as-grown oxides would be at NA and ^{16}O-dominant i.e., 99.8% ^{16}O, 0.2% ^{18}O) and interpret oxygen ingress and mobility from the reactor environment. Elemental and isotopic compositions were shown to be consistent between duplicate APT specimens in the same condition (Table S1, Supporting Information). One specimen from each experiment is shown in the main text as the representative sample; elemental and isotopic analyses of the remaining specimens are provided in Figure S4, Supporting Information.

STEM Analyses: STEM-HAADF images were acquired on a probe-corrected JEOL GrandARM-300F microscope operating at 300 kV, with a convergence semi-angle of 29.7 mrad and a collection angle range of 75–515 mrad.

Theory Calculations: The VASP package[55] was used to perform density functional theory (DFT) simulations of defective and Sr-doped LSFO materials. All the simulations used the generalized gradient approximation (GGA) as parametrized in the PBEsol functional[56] in combination with the Hubbard correction[57] ($U_{eff} = U–J = 4$ eV) to better describe the Coulomb repulsion of the 3d electrons of the Fe atoms.[58] All the simulations used a cutoff energy of 550 eV and a 2 × 2 × 2 Monkhorst-Pack *k*-points mesh to sample the Brillouin zone. The total energy was converged to 10^{-6} eV per cell, the force components were relaxed to 10^{-5} eV Å^{-1}, and all the simulations used spin-polarization.

The generation of a 50% Sr-doped LSFO (i.e., $La_{0.5}Sr_{0.5}FeO_3$) unit cell used as a starting structure a 2 × 2 × 2 supercell (160 atoms) of pure LFO compound. The relaxation of the orthorhombic (space group Pbnm #62) LFO as a G-type anti-ferromagnetic materials yielded lattice parameters a = 5.54 Å (–0.72%), b = 5.54 Å (–0.60%), and c = 7.80 Å (–0.72%), in good agreement with the experimental lattice parameters a = 5.55 Å, b = 5.57 Å, and c = 7.85 Å.[59] The structure of a 50% La/Sr mixed compound was generated using the special quasirandom structure (SQS) code available from the alloy theoretic automated toolkit (ATAT).[60] Once the lattice parameters and coordinates of the 50% Sr-doped structure were optimized, one oxygen vacancy was introduced into the structure and only the coordinates were relaxed while the lattice parameters were kept fixed at their optimized values.

The temperature and O_2 partial pressure (p_{O_2}) dependence of the Gibbs free energy, $\Delta G_f(T,p_{O_2})$, of oxygen vacancy was determined by ab initio thermodynamics simulations, following the equation (Eqn. 1):

$$\Delta G_f\left(T,p_{O_2}\right)=\left(E^T_{V_O}+E^{ZPE}_{V_O}+\Delta\mu(T)_{V_O}\right)-\left(E^T_{perf}+E^{ZPE}_{perf}+\Delta\mu(T)_{perf}\right)+\frac{1}{2}\left(E^T_{O_2}+E^{ZPE}_{O_2}+\Delta\mu_{O_2}\left(T,p_{O_2}\right)\right) \quad (1)$$

where $E^T_{V_O}$ and E^T_{perf} are the DFT total energies of the $La_{0.5}Sr_{0.5}FeO_3$ solid systems with and without oxygen vacancy while $E^{ZPE}_{V_O}$ and E^{ZPE}_{perf} are the zero-point-energies of the defective and defect-free system. $E^T_{O_2}$, $E^{ZPE}_{O_2}$, and $\Delta\mu_{O_2}(T,p_{O_2})$ are respectively the total DFT energy, the zero-point-energy, and the temperature and O_2 partial pressure dependent chemical potential of oxygen. The DFT total energy of molecular O_2 was corrected to the experimental atomization energy of the gaseous species[61] leading to an energy correction of 1.482 eV. To account for temperature effect in $La_{0.5}Sr_{0.5}FeO_3$, $\Delta\mu(T)_{V_O}$ and $\Delta\mu(T)_{perf}$ are the temperature-dependent chemical potentials of the system with and without an oxygen vacancy. All the temperature-dependent chemical potentials were calculated using the following relation (Eqn. 2):

$$\Delta\mu(T)=\left(H(T)-H^\circ(298.15)\right)-TS \quad (2)$$

where $H(T)$ and $H^\circ(298.15)$ are the system enthalpy at a temperature T and at $T = 298.15$ K, and S is the entropy. In the simulations, the phonon frequencies were calculated using the Phonopy code.[62]

The simulations of O vacancy migration pathways used the CINEB method as implemented in the transition state tools for VASP.[63]

Supporting Information

Supporting Information is available from the Wiley Online Library or from the author.

Acknowledgements

This research was supported by the Chemical Dynamics Initiative/ Investment, under the Laboratory Directed Research and Development (LDRD) Program at Pacific Northwest National Laboratory (PNNL). D.K.S. acknowledges support from the U.S. Department of Energy (DOE) Office of Science, Basic Energy Sciences, Materials Science, and Engineering Division for supporting APT data analysis and interpretation. PNNL is a multi-program national laboratory operated for the U.S. DOE by Battelle Memorial Institute under Contract No. DE-AC05-76RL01830. The growth of thin film samples was supported by DOE Office of Science, Basic Energy Sciences under award #10122. Experimental sample preparation and APT analysis was performed at the Environmental Molecular Sciences Laboratory, a national scientific user facility sponsored by the Department of Energy's Office of Biological and Environmental Research and located at PNNL. STEM data was collected in the Radiological Microscopy Suite, located in the Radiochemical Processing Laboratory at PNNL. The authors would also like to thank Dr. Blas Uberuaga (Los Alamos National Laboratory) for helpful discussions on the simulations.

Conflict of Interest

The authors declare no conflict of interest.

Author Contributions

S.D.T. and K.H.Y. contributed equally to this work. S.D.T., K.H.Y., and S.R.S. conceived and developed the project plan. L.W. and Y.D. prepared the thin film samples. S.D.T., K.H.Y., E.J.K., S.N., and D.K.S. conducted APT analysis. B.M. conducted STEM sample preparation and imaging. M.S. conducted theory calculations. All authors contributed to the writing and editing of the manuscript.

Data Availability Statement

All relevant data are presented in the main text or Supporting Information. STEM, APT, and DFT data can be made available upon request by contacting the authors.

Keywords

atom exchange, atom probe tomography, density functional theory, oxygen diffusion, perovskites

Received: October 26, 2022
Revised: December 19, 2022
Published online:

[1] P. K. Davies, H. Wu, A. Y. Borisevich, I. E. Molodetsky, L. Farber, *Annu. Rev. Mater. Res.* **2008**, *38*, 369.
[2] M. Dawber, K. M. Rabe, J. F. Scott, *Rev. Mod. Phys.* **2005**, *77*, 1083.
[3] L. Wang, K. A. Stoerzinger, L. Chang, J. Zhao, Y. Li, C. S. Tang, X. Yin, M. E. Bowden, Z. Yang, H. Guo, L. You, R. Guo, J. Wang, K. Ibrahim, J. Chen, A. Rusydi, J. Wang, S. A. Chambers, Y. Du, *Adv. Funct. Mater.* **2018**, *28*, 1803712.
[4] J. Liu, E. Jia, L. Wang, K. A. Stoerzinger, H. Zhou, C. S. Tang, X. Yin, X. He, E. Bousquet, M. E. Bowden, A. T. S. Wee, S. A. Chambers, Y. Du, *Adv. Sci.* **2019**, *6*, 1901073.
[5] L. Wang, P. Adiga, J. Zhao, W. S. Samarakoon, K. A. Stoerzinger, S. R. Spurgeon, B. E. Matthews, M. E. Bowden, P. V. Sushko, T. C. Kaspar, G. E. Sterbinsky, S. M. Heald, H. Wang, L. W. Wangoh, J. Wu, E. J. Guo, H. Qian, J. Wang, T. Varga, S. Thevuthasan, Z. Feng, W. Yang, *Nano Lett.*. **2021**, *21*, 8324.
[6] Y. Zhou, X. Guan, H. Zhou, K. Ramadoss, S. Adam, H. Liu, S. Lee, J. Shi, M. Tsuchiya, D. D. Fong, S. Ramanathan, *Nature* **2016**, *534*, 231.
[7] R. Comes, S. Chambers, *Phys. Rev. Lett.* **2016**, *117*, 226802.
[8] H. Shen, T. Xue, Y. Wang, G. Cao, Y. Lu, G. Fang, *Mater. Res. Bull.* **2016**, *84*, 15.
[9] K. A. Stoerzinger, L. Wang, Y. Ye, M. Bowden, E. J. Crumlin, Y. Du, S. A. Chambers, *J. Mater. Chem. A* **2018**, *6*, 22170.
[10] H. Chang, E. Bjørgum, O. Mihai, J. Yang, H. L. Lein, T. Grande, S. Raaen, Y. A. Zhu, A. Holmen, D. Chen, *ACS Catal.* **2020**, *10*, 3707.
[11] J. Hwang, R. R. Rao, L. Giordano, Y. Katayama, Y. Yu, Y. Shao-Horn, *Science* **2017**, *358*, 751.
[12] Y. S. Zheng, M. Zhang, Q. Li, Y. A. Zhu, Z. J. Sui, D. Chen, X. G. Zhou, *J. Phys. Chem. C* **2019**, *123*, 275.
[13] T. Ishigaki, S. Yamauchi, K. Kishio, J. Mizusaki, K. Fueki, *J. Solid State Chem.* **1988**, *73*, 179.
[14] J. E. ten Elshof, M. H. R. Lankhorst, H. J. M. Bouwmeester, *J. Electrochem. Soc.* **1997**, *144*, 1060.
[15] M. Li, Y. Wang, Y. Wang, F. Chen, C. Xia, *ACS Appl. Mater. Interfaces* **2014**, *6*, 11286.
[16] J. Liu, E. Jia, K. A. Stoerzinger, L. Wang, Y. Wang, Z. Yang, D. Shen, M. H. Engelhard, M. E. Bowden, Z. Zhu, S. A. Chambers, Y. Du, *J. Phys. Chem. C* **2020**, *124*, 15386.
[17] S. B. Adler, X. Y. Chen, J. R. Wilson, *J. Catal.* **2007**, *245*, 91.
[18] J. Ascolani-Yael, A. Montenegro-Hernández, D. Garcés, Q. Liu, H. Wang, K. Yakal-Kremski, S. Barnett, L. Mogni, *J. Phys. Energy* **2020**, *2*, 042004.

[19] L. Zhou, J. H. Mason, W. Li, X. Liu, *Renew Sustain Energy Rev* **2020**, *134*, 110320.
[20] T. Horita, Y. Xiong, H. Kishimoto, K. Yamaji, M. E. Brito, H. Yokokawa, *J. Electrochem. Soc.* **2010**, *157*, B614.
[21] J. Y. Kim, N. L. Canfield, L. A. Chick, K. D. Meinhardt, V. L. Sprenkle, *Advances in Solid Oxide Fuel Cells III: Ceramic Engineering and Science Proceedings*, Wiley, New York **2005**, *26*, 4.
[22] R. Wang, Z. Sun, Y. Lu, S. Gopalan, S. N. Basu, U. B. Pal, *J. Power Sources* **2020**, *476*, 228743.
[23] T. Ishigaki, S. Yamauchi, K. Fueki, H. Naitoh, T. Adachi, *Secondary Ion Mass Spectrometry SIMS IV*, Springer, Berlin, Heidelberg **1984**.
[24] N. Mahato, A. Banerjee, A. Gupta, S. Omar, K. Balani, *Prog. Mater. Sci.* **2015**, *72*, 141.
[25] K. H. Yano, A. A. Kohnert, A. Banerjee, D. J. Edwards, E. F. Holby, T. C. Kaspar, H. Kim, T. G. Lach, S. D. Taylor, Y. Wang, B. P. Uberuaga, D. K. Schreiber, *Chem. Mater.* **2021**, *33*, 2307.
[26] S. D. Taylor, J. Liu, X. Zhang, B. W. Arey, L. Kovarik, D. K. Schreiber, D. E. Perea, K. M. Rosso, *Proc. Natl. Acad. Sci. U. S. A.* **2019**, *116*, 2866.
[27] F. Baiutti, F. Chiabrera, D. Diercks, A. Cavallaro, L. Yedra, L. López-Conesa, S. Estradé, F. Peiró, A. Morata, A. Aguadero, A. Tarancón, *Adv. Mater.* **2021**, *33*, 2105622.
[28] K. Schweinar, B. Gault, I. Mouton, O. Kasian, *J. Phys. Chem. Lett.* **2020**, *11*, 5008.
[29] S. V. Lambeets, E. J. Kautz, M. G. Wirth, G. J. Orren, A. Devaraj, D. E. Perea, *Top. Catal.* **2020**, *63*, 1606.
[30] B. Gault, D. W. Saxey, M. W. Ashton, S. B. Sinnott, A. N. Chiaramonti, M. P. Moody, D. K. Schreiber, *New J. Phys.* **2016**, *18*, 033031.
[31] A. Devaraj, R. Colby, W. P. Hess, D. E. Perea, S. Thevuthasan, *J. Phys. Chem. Lett.* **2013**, *4*, 993.
[32] M. Bachhav, F. Danoix, B. Hannoyer, J. M. Bassat, R. Danoix, *Int. J. Mass Spectrom.* **2013**, *335*, 57.
[33] M. Bachhav, R. Danoix, F. Danoix, B. Hannoyer, S. Ogale, F. Vurpillot, *Ultramicroscopy* **2011**, *111*, 584.
[34] S. D. Taylor, J. Liu, B. W. Arey, D. K. Schreiber, D. E. Perea, K. M. Rosso, *J. Phys. Chem. C* **2018**, *122*, 3903.
[35] T. C. Kaspar, S. D. Taylor, K. H. Yano, T. G. Lach, Y. Zhou, Z. Zhu, E. K. Still, P. Hosemann, S. R. Spurgeon, D. K. Schreiber, *Adv. Mater. Interfaces* **2021**, *8*, 2001768.
[36] A. M. Ritzmann, A. B. Muñoz-García, M. Pavone, J. A. Keith, E. A. Carter, *Chem. Mater.* **2013**, *25*, 3011.
[37] Y. Orikasa, T. Nakao, M. Oishi, T. Ina, A. Mineshige, K. Amezawa, H. Arai, Z. Ogumi, Y. Uchimoto, *J. Mater. Chem.* **2011**, *21*, 14013.
[38] M. Søgaard, P. V. Hendriksen, M. Mogensen, *J. Solid State Chem.* **2007**, *180*, 1489.
[39] K. H. Yano, A. A. Kohnert, T. C. Kaspar, S. D. Taylor, S. R. Spurgeon, H. Kim, Y. Wang, B. P. Uberuaga, D. K. Schreiber, *J. Phys. Chem. C* **2021**, *125*, 27820.
[40] B. P. Geiser, D. J. Larson, E. Oltman, S. Gerstl, D. Reinhard, T. F. Kelly, T. J. Prosa, *Microsc. Microanal.* **2009**, *15*, 292.
[41] H. J. T. Ellingham, *J. Soc. Chem. Ind.* **1944**, *63*, 125.
[42] W. H. Blades, P. Reinke, *ACS Appl. Mater. Interfaces* **2018**, *10*, 43219.
[43] C. M. Wang, A. Genc, H. Cheng, L. Pullan, D. R. Baer, S. M. Bruemmer, *Sci. Rep.* **2015**, *4*, 3683.
[44] L. Luo, L. Zou, D. K. Schreiber, D. R. Baer, S. M. Bruemmer, G. Zhou, C. M. Wang, *Scr. Mater.* **2016**, *114*, 129.
[45] J. W. Park, C. J. Altstetter, *Metall. Trans. A* **1987**, *18*, 43.
[46] Wi.C. Hagel, *J. Am. Ceram. Soc.* **1965**, *48*, 70.
[47] A. C. S. Sabioni, B. Lesage, A. M. Huntz, J. C. Pivin, C. Monty, *Philos. Mag. A* **1992**, *66*, 333.
[48] D. L. Douglass, *Corros. Sci.* **1968**, *8*, 665.
[49] G. C. Wood, I. G. Wright, J. M. Ferguson, *Corros. Sci.* **1965**, *5*, 645.
[50] E. J. Kautz, B. Gwalani, S. V. M. Lambeets, L. Kovarik, D. K. Schreiber, D. E. Perea, D. Senor, Y. S. Liu, A. K. Battu, K. P. Tseng, S. Thevuthasan, A. Devaraj, *Npj Mater. Degrad.* **2020**, *4*, 29.
[51] A. Devaraj, D. J. Barton, C. Li, S. V. Lambeets, T. Liu, A. Battu, S. Vaithiyalingam, S. Thevuthasan, F. Yang, J. Guo, T. Li, Y. Ren, L. Kovarik, D. E. Perea, M. L. Sushko, *Adv. Mater. Interfaces* **2022**, *9*, 2270115.
[52] E. J. Kautz, S. V. Lambeets, J. Royer, D. E. Perea, S. S. Harilal, A. Devaraj, *Scr. Mater.* **2022**, *212*, 114528.
[53] K. Thompson, D. Lawrence, D. J. Larson, J. D. Olson, T. F. Kelly, B. Gorman, *Ultramicroscopy* **2007**, *107*, 131.
[54] L. A. Giannuzzi, J. L. Drown, S. R. Brown, R. B. Irwin, F. A. Stevie, *Microsc. Res. Tech.* **1998**, *41*, 285.
[55] G. Kresse, J. Furthmüller, *Phys Rev B Condens Matter Mater Phys* **1996**, *54*, 11169.
[56] J. P. Perdew, A. Ruzsinszky, G. I. Csonka, O. A. Vydrov, G. E. Scuseria, L. A. Constantin, X. Zhou, K. Burke, *Phys. Rev. Lett.* **2008**, *100*, 136406.
[57] S. Dudarev, G. Botton, *Phys. Rev. B: Condens. Matter Mater. Phys.* **1998**, *57*, 1505.
[58] V. I. Anisimov, F. Aryasetiawan, A. I. Lichtenstein, *J. Phys. Condens. Matter* **1997**, *9*, 767.
[59] S. M. Selbach, J. R. Tolchard, A. Fossdal, T. Grande, *J. Solid State Chem.* **2012**, *196*, 249.
[60] A. Van De Walle, P. Tiwary, M. De Jong, D. L. Olmsted, M. Asta, A. Dick, D. Shin, Y. Wang, L. Q. Chen, Z. K. Liu, *CALPHAD: Comput. Coupling Phase Diagrams Thermochem.* **2013**, *42*, 13.
[61] J. P. Perdew, K. Burke, M. Ernzerhof, *Phys. Rev. Lett.* **1997**, *78*, 1396.
[62] A. Togo, I. Tanaka, *Scr. Mater.* **2015**, *108*, 1.
[63] G. Henkelman, B. P. Uberuaga, H. Jónsson, *J. Chem. Phys.* **2000**, *113*, 9901.